D3.5

Impact of stable defect configurations on the electrical performances of OTS selectors

Enrico Piccinini, Andrea Padovani, Linda-Sheila Medondjio, Sergiu Clima, Xu He, Francesco Tavanti, Amine Slassi, Pablo Ordejón, and Arrigo Calzolari

Document information

Project acronym:	INTERSECT
Project full title:	Interoperable Material-to-Device simulation box for disruptive electronics
Research Action Project type:	Accelerating the uptake of materials modelling software (IA)
EC Grant agreement no.:	814487
Project starting / end date:	1st January 2019 (M1) / 30th April 2022 (M40)
Website:	www.intersect-project.eu
Final version:	29/04/2022
Deliverable No.:	D3.5
Responsible participant:	AMAT (participant number 8)
Contributing Consortium members:	IMEC, ICN2, CNR
Due date of deliverable:	30/04/2022
Actual submission date:	29/04/2022
Dissemination level:	PU - Public

Authors: E. Piccinini, A. Padovani, L.-S. Medondjio, S. Clima, X. He, F. Tavanti, A. Slassi, P. Ordejón, and A. Calzolari

To be cited as: E. Piccinini, A. Padovani, L.-S. Medondjio, S. Clima, H. Xu, F. Tavanti, A. Slassi, P. Ordejón, and A. Calzolari (2022): Impact of stable defect configurations on the electrical performances of OTS selectors. Deliverable D3.5 of the H2020 project INTERSECT (final version as of 29/04/2022). EC grant agreement no: 814487, AMAT, Reggio Emilia, Italy

Disclaimer:

This document's contents are not intended to replace consultation of any applicable legal sources or the necessary advice of a legal expert, where appropriate. All information in this document is provided "as is" and no guarantee or warranty is given that the information is fit for any particular purpose. The user, therefore, uses the information at its sole risk and liability. For the avoidance of all doubts, the European Commission has no liability in respect of this document, which is merely representing the authors' view.

Versioning and Contribution History

Version	Date	Modified by	Modification reason
v.01	15/04/2022	Enrico Piccinini, Andrea Padovani	First version
v.02	19/04/2022	Linda-Sheila Medondjio	First Revision
v.03	23/04/2022	Arrigo Calzolari	Second Revision
v04	28/04/2022	Pablo Ordejón	Third Revision

Contents

[1] Acronyms are marked in purple in the text and defined at the end of the document.

Executive Summary

This deliverable reports on the activities carried out within Task 3.4 and, along with D3.2[2] complete the research activity on pilot case 2 about chalcogenide Ovonic Threshold Switching (OTS) selector devices. While the previous D3.2 report focused on the device-to-material (D2M) approach to materials characterization, the document focuses on the material-to-device (M2D) pathway for the device optimization.

This report provides a description of the use of the material cycle of the Interoperable Materials to Device (IM2D) Simulation box to investigate the effects of material and defect properties, calculated through Density Functional Theory (DFT), on the performance of GeSe-based OTS devices.

The task activities rely on the use of DFT calculations to determine key material properties (e.g., bandgap, DOS, work-function) and identify the relevant atomic and electronic features in GeSe films with different stoichiometry and doping concentrations.

Results obtained from DFT are then used as inputs in OTS device simulations, performed with the Ginestra® platform connected to the IM2D box. The Ginestra® OTS module is used to simulate the current-voltage characteristic of the device and evaluate the impact that changes in material doping and composition (typically accompanied by changes in bandgap and atomic defects) have on its switching characteristic (current, switching voltage).

1. Introduction

One goal behind the INTERSECT project is to set up an Interoperable Materials to Device framework able to integrate materials modeling codes to device-oriented simulators. This report focuses on the pilot case for the development of solutions for OTS materials for selector applications. More specifically, it addresses the material-to-device workflow, which consists in the use of DFT methods to compute material properties to be used in device-level simulations to understand (and *predict*) their impact on the device electrical behaviour.

The calculated materials properties, resulting from extensive DFT simulations, are used as input for the device simulation by Ginestra®. In the present case, DFT results have been

[2] https://intersect-project.eu/wp-content/uploads/2022/04/D3.2.pdf

performed by both the simulator engines included in the IM2D box, namely SIESTA and Quantum ESPRESSO (QE). In this work, we exploited the automation and semantic capability of the IM2D infrastructure, provided by AiiDA and SimPhoNy codes, as described in the technical reports of WP1 and WP2.

Among the novel technologies which are being explored for neuromorphic computing, the class of switching memories, such as the phase-change memories (PCMs) [1] or resistive random-access memories (RRAMs) [2], is among the most investigated by the semiconductor industry. These elements are incorporated in complex memory cells [3], which include 3D cross-point arrays of switching memory interconnected by selectors, which control the accessibility and quality of data transmission within and outside the entire cell. Selectors are dynamical switches to the encoding mode with possibly lowest bit error rate, according to the current type of the transmission [4].

Here, we focus on the electrical properties of amorphous GeSe compounds that have been proposed as promising (ovonic) switching materials for non-volatile memory devices and OTS selectors. The experimental results generated by the IMEC team (see D3.2) indicate that GeSe exhibits ovonic electrical switching [5] and that even moderate modulation of the stoichiometry ratio or doping affects the electrical response of the device, in terms both of I-V characteristics and of power dissipation (D3.2). Rather, the origins of this behaviour are still unknown. In the Sections below we extensively investigate the combined effect of stoichiometry, dopant species and doping amount on the electronic properties and transport response of GeSe-based OTS selectors.

2. The Material-to-Device (M2D) workflow of the IM2D box

Figure 1 shows a schematic representation of the material-to-device workflow of the IM2D simulation box, whose main purpose is to optimize and guide device design by understanding and predicting its performance starting from DFT-computed material properties.

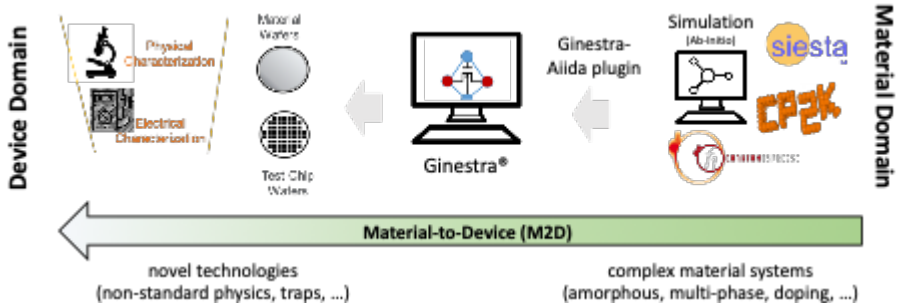

Figure 1 – Schematic representation of the M2D workflow.

The workflow starts from the material domain, where DFT codes are used to compute key properties of the material system of interest (for example: material properties such as the bandgap, trap properties, metal-material interface, etc.). The results of DFT calculations represent the input (they can be gathered automatically through the Ginestra-Aiida plugin developed within the project) to subsequent device simulations. The final goal is to evaluate the impact of the material properties on the device performance and electrical characteristics. This material-to-device simulation flow enables a virtualization of the device fabrication process that allows us to understand the impact of process and material variations and identify the most promising process and technology solutions. Semiconductor companies may then fabricate and characterize only the identified solutions, thus reducing costs (for technology development and fabrication) and time-to-market.

3. DFT Calculations of Material and Defect Properties of Doped GeSe Films

The GeSe films in the OTS selectors are in the amorphous phase. Given the intrinsic disordered nature of the amorphous materials, the understanding of the interplay among local-order structures, dopants, and electronic states requires the capability of treating large systems at the atomistic level and of having access to the corresponding electronic structure. In the absence of specific experimental results on the atomic structure of the amorphous phase at the atomistic level, the identification of reliable atomic structures is a major challenge for theory. In order to obtain realistic models of the amorphous structure without resorting to phenomenological or empirical potentials, we carried out two independent sets of simulations obtained via different multi-scale approaches, which best exploit the different computational characteristics of SIESTA and QE DFT codes. This activity has been carried out in close collaboration between the ICN2 and CNR teams.

3.1 Approach 1: Markov chain Monte Carlo + melting-and-quenching protocol

A series of compositions of Ge_xSe_{1-x} with x=0.4, 0.5, 0.6 has been generated by the Markov Chain Monte Carlo followed by a melting-and-quenching method performed with the ab initio molecular dynamics (MD) implemented in the SIESTA code.

3.1.1. Structure generation

We use the Markov chain Monte Carlo simulation to generate the starting amorphous structure of the a-$Ge_{50}Se_{50}$ stoichiometry, from a random distribution of N=336 atoms in a cubic box of L=21 Ang of side. A repulsive interaction between atoms is added to make the distribution of the atoms more homogeneous in the cell. With this, we performed Markov chain Monte Carlo to generate structures with the target coordination numbers as the initial input for the MD simulations.

Starting from these initial structures, the amorphous models have been obtained through melting-and-quenching cycles, carried on by using ab initio MD, with SIESTA. The quenching step is particularly critical to obtain trustable amorphous results. We found (see also D3.2) that (i) the relaxation of volume under constant pressure, (ii) the use of a relatively large basis set (DZP) during the quenching procedure, and (iii) a low quenching rate are necessary steps for the building of realistic GeSe amorphous structures. The details of the quenching-and-melting approach are summarized in Table I. The structural features of the resulting models, including the radial distribution function (RDF), the angle distribution function (ADF), and the coordination number distributions have been calculated.

3.1.2. Results

As an initial step, we considered the case of undoped, stoichiometric a-GeSe. We found that the a-GeSe generated starting from 4:2 coordinated initial structure is 3:3 coordinated, as its corresponding GeSe crystalline phase. We validated our model for a system with 336 atoms. The results indicate that the electronic features in the proximity of the band gap are not size-dependent, as confirmed by the comparison with larger systems made of 500, 1000 and 4032 atoms generated by the CNR group, by using classical MD simulations (see comparison below). The radial distribution function analysis is summarized in Figure 2. We got few to non-existent Ge-Ge clustering in our generated amorphous geometries following the same protocol previously used by our collaborators at IMEC (D3.2), but quenched 2 times slower. This results in a cleaner electronic band gap. We have also noticed a strong and narrow Ge-Se first-neighbor shell only slightly shifted from the GeSe crystalline phase. Quenching the melted structure leads to the breakage of the homopolar Se-Se bonds.

Table I: Melt-Quench Protocol for generating of the amorphous structures.

Initial Structure	Generate initial structure with MCMC (336 atoms). Then Relax structure (cell and atom coordinates)
Melt	6 ps at 1200 K, SZ, NPT + 6 ps at 1200 K NPT
Quench1	1200K-800K, 3ps in total, 1fs per step, τ relax =1000 fs: SZ, NPT
Quench 2	800K-400K, 3ps in total, 1fs per step, τ relax = 750 fs; SZ, NPT
Quench 3	400K-400K, 3ps in total, 1fs per step, τ relax = 750 fs; DZP, NPT

We have also done calculations with non-stoichiometric compositions: a-Ge_xSe_{1-x}. The results for x=0.4 and for x=0.6 show that there is Ge and Se clustering in Ge and Se -rich structures, respectively; the Ge-rich structures tend to have larger coordination numbers, opposite to the Se-rich structures. The electronic structures of these samples have been calculated. The inverse partition ratio (IPR) and the Density of States (DOS) are summarized in Figure 3. The mobility gap decreases with x, while in the x=0.6 samples, large numbers of in-gap localized states tend to form. Preliminary results on the thermal transport through a-GeSe have been reported in D2.7[3].

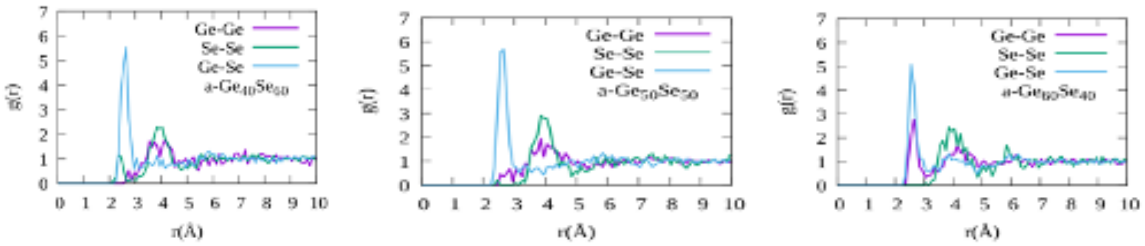

[3] Available on INTERSECT website https://intersect-project.eu/project-reports/ after submission.

Figure 2. Radial distribution function for undoped a-GeSe systems at different stoichiometries.

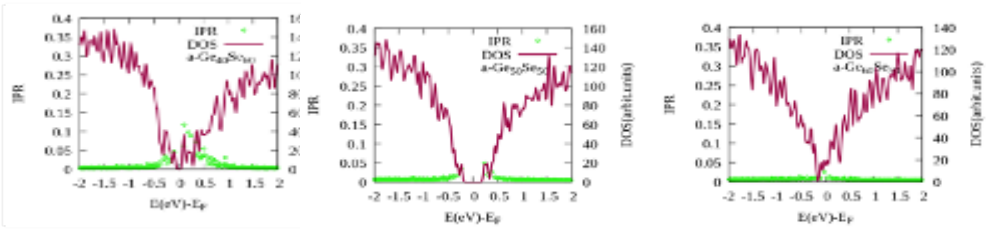

Figure 3. Electronic DOS and IPR for undoped a-GeSe systems at different stoichiometries.

In a second step, we applied this approach to simulate a series of doped a-Ge_xSe_{1-x} systems, by varying both the stoichiometry (x=0.4, 0.5, 0.6), the dopants (Si, S, As, P, Te), and their concentrations (0%, 1%, 3%, 5%, 7%, 10%, 15%). Some structural features, including the radial distribution function, the angle distribution function, the persistence homology, and the coordination number distributions have been calculated. The results show that there are Ge and Se clustering in Ge and Se-rich structures, respectively, as in the undoped cases; the Ge-rich structures tend to have larger coordination numbers, opposite to the Se-rich structures. The electronic property features, including the Crystal Orbital Hamilton Populations (COHP), the IPR, the total and the local DOS have been analyzed and interconnected to the corresponding structural features. To that end, we used methods based on the conventional ways of chemical environment analysis like the COHP that correspond to the derivative of the band energy with respect to the strength of the bond. The n'th moment of the PDOS gives a description of the states and provides some chemical intuition about how the electronic structure is related to the chemical environment. We further defined some global descriptors such as the chemical composition, Density, Global radial/angle distribution functions, and some local descriptors such as the specie at the atomic site, electronegativity, the Mulliken charge analysis, number of valence electrons of the atom, the local RDF/ADF, which is centred at one atom. The dopants behave similarly with their iso-valent hosting ions with some delicate differences, of which the structural and electronic origin has been also explored. These results will provide guidelines on the improvement of the memory switching performance of a-GeSe.

For the sake of brevity, we will show in Figures 4-8 the results for the structural analysis obtained for the doped a-Ge_xSe_{1-x} systems for all the dopants (Si, S, As, P, Te), and all their concentrations (1%, 3%, 5%, 7%, 10%, 15%), but only for the stoichiometric case (x=0.5).

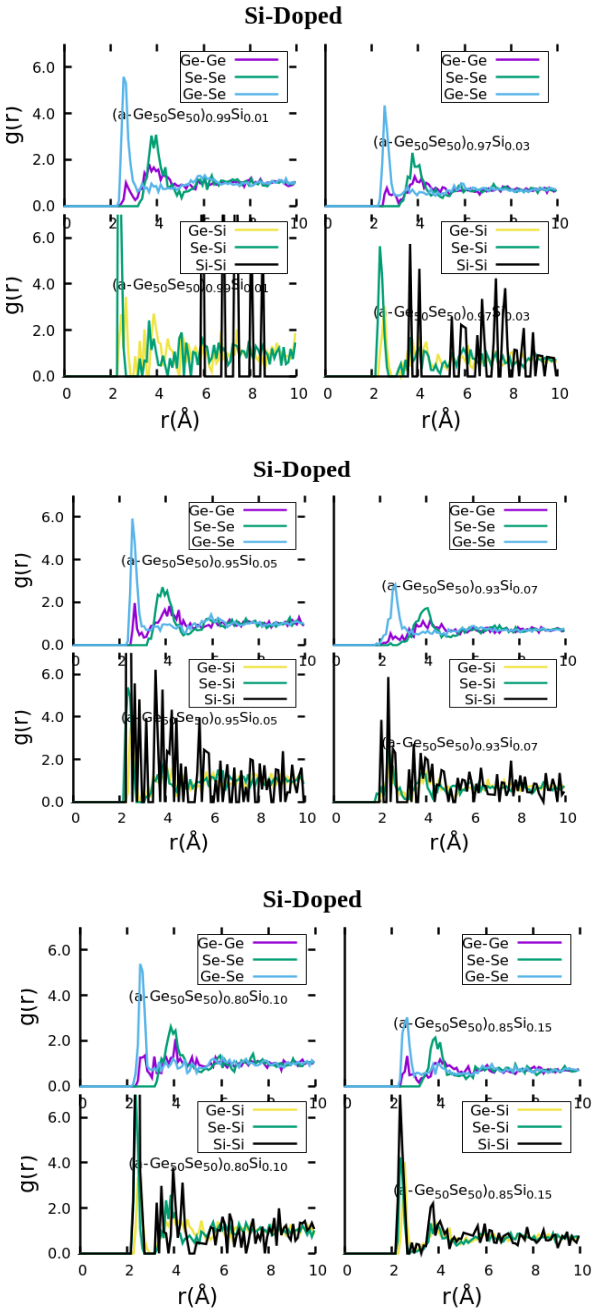

Figure 4. Radial distribution function for Si-doped a-GeSe system at different dopant concentrations.

Increasing the Si-Dopant concentration leads to an increase of the Ge-Ge clustering. This could be seen from the Ge-Si RDF first neighbor shell peak at about 2.5 Ang which is similar to

the Ge-Ge clustering. Silicon behaves similarly to Ge when interacting with Se (Si has similar electronic configuration as Ge).

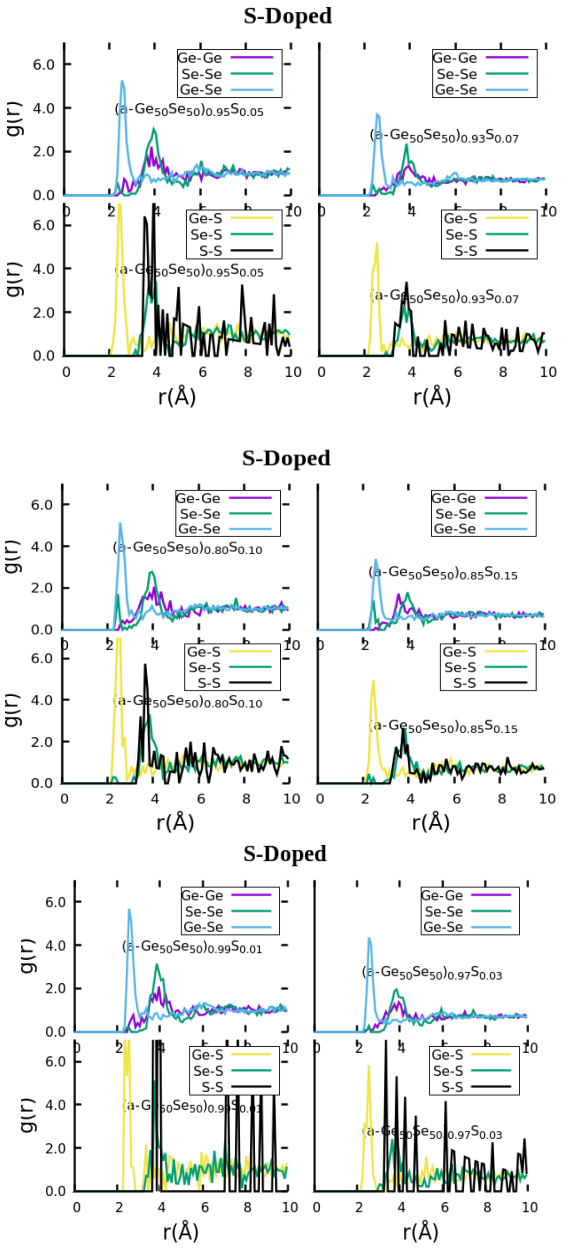

Figure 5. Radial distribution function for S-doped a-GeSe system at different dopant concentrations.

For S dopants, the Ge-S RDF is similar to the Ge-Se RDF. Increasing the S dopant concentration leads to a Se-Se clustering at about 2.3 Ang initially not present in the undoped a-$Ge_{50}Se_{50}$ Se-Se RDF. We notice the Se-S first neighbour shell clustering at about 2.3 Ang similar to Se-Se.

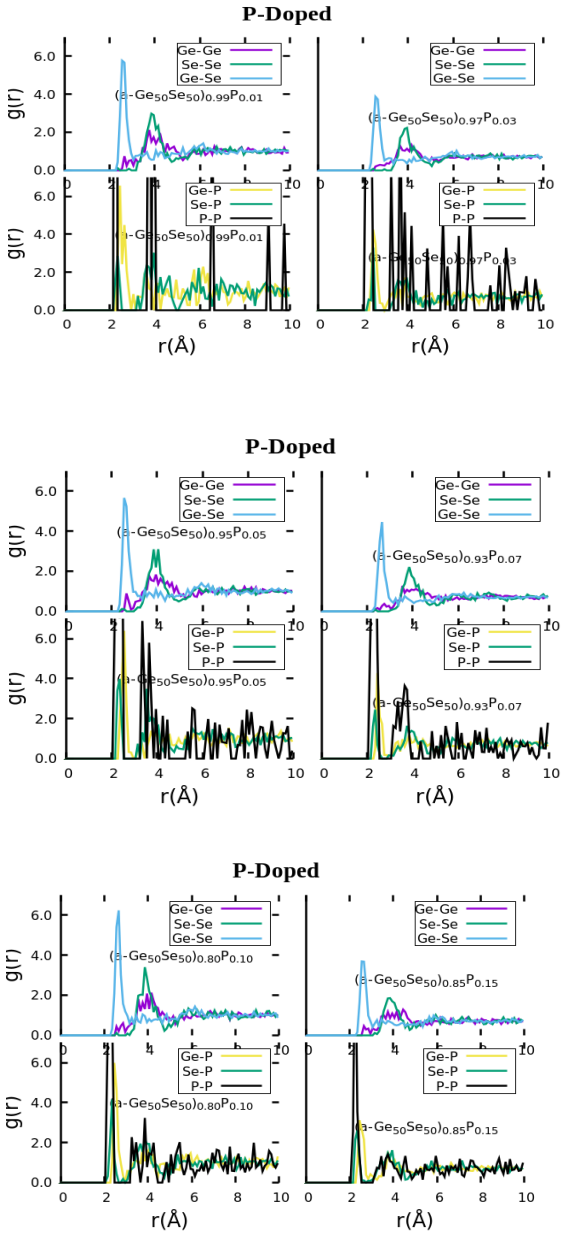

Figure 6. Radial distribution function for P-doped a-GeSe system at different dopant concentrations.

P seems to interact both with Se and Ge similarly (Ge-P RDF is similar to Se-P RDF). The inclusion of P dopants to the a-Ge50Se50 does not change the Ge-Ge, Ge-Se, and the Se-Se RDF significantly.

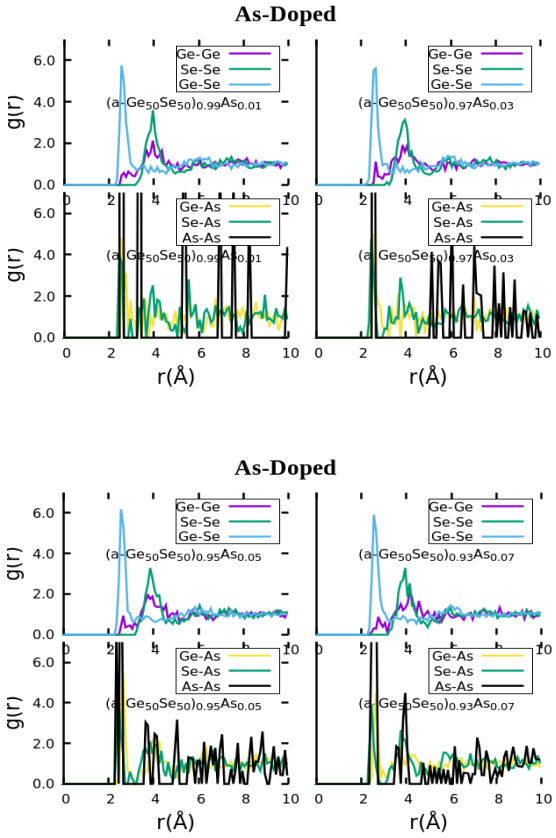

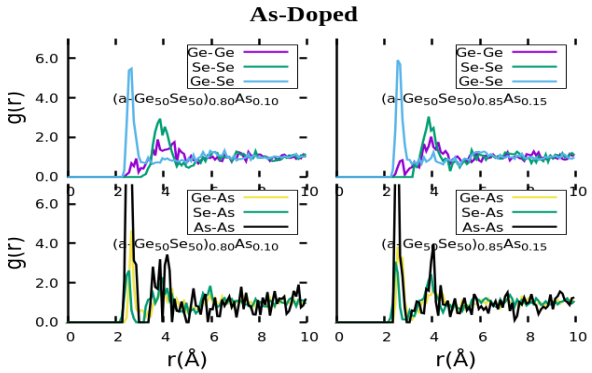

Figure 7. Radial distribution function for As-doped a-GeSe system at different dopant concentrations.

Arsenic dopant does not change the Ge-Ge, Ge-Se, and Se-Se RDF significantly.

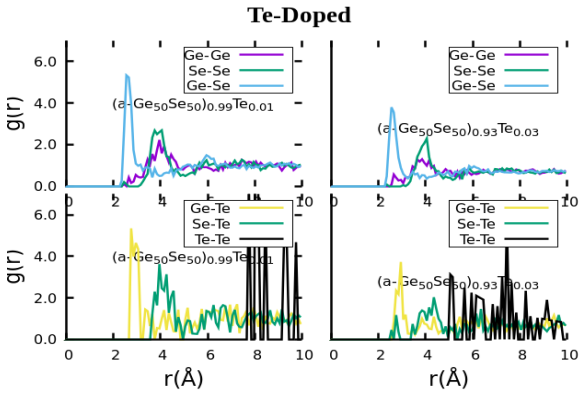

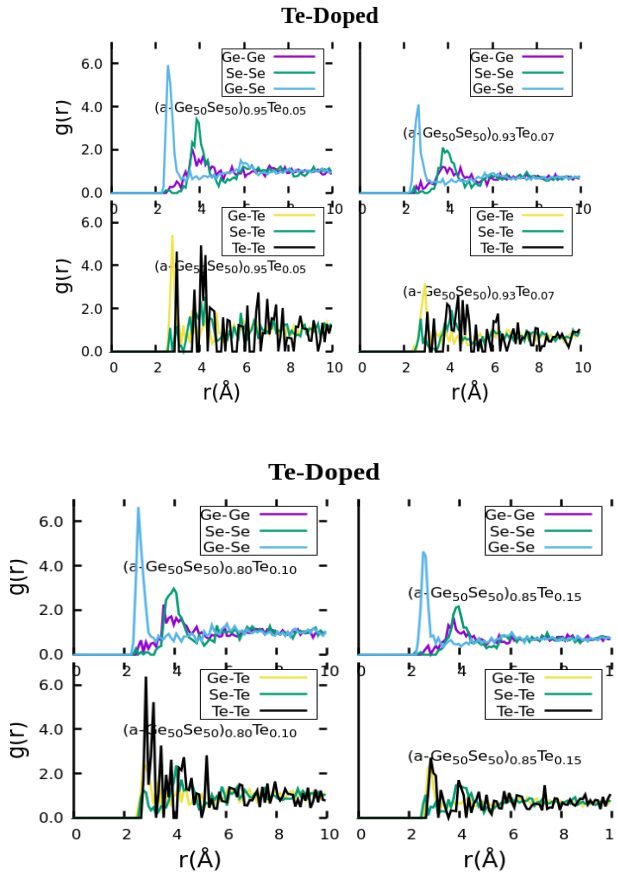

Figure 8. Radial distribution function for Te-doped a-GeSe system at different dopant concentrations.

The addition of Te dopants into a-Ge50Se50 favours a Se-Se clustering at about 2.5 Ang. We notice a Se-Te peak at about 2.5 Ang. The Ge-Te RDF is similar to the Ge-Se one.

For the a-$Ge_{60}Se_{40}S_{15}$ and a-$Ge_{40}Se_{60}Si_{15}$, we choose a single in-gap state in which the S and the Si dopants atoms are involved, respectively. The corresponding local density of states (top panels) and the total DOS (bottom panels) are reported in Figures 9 and 10.

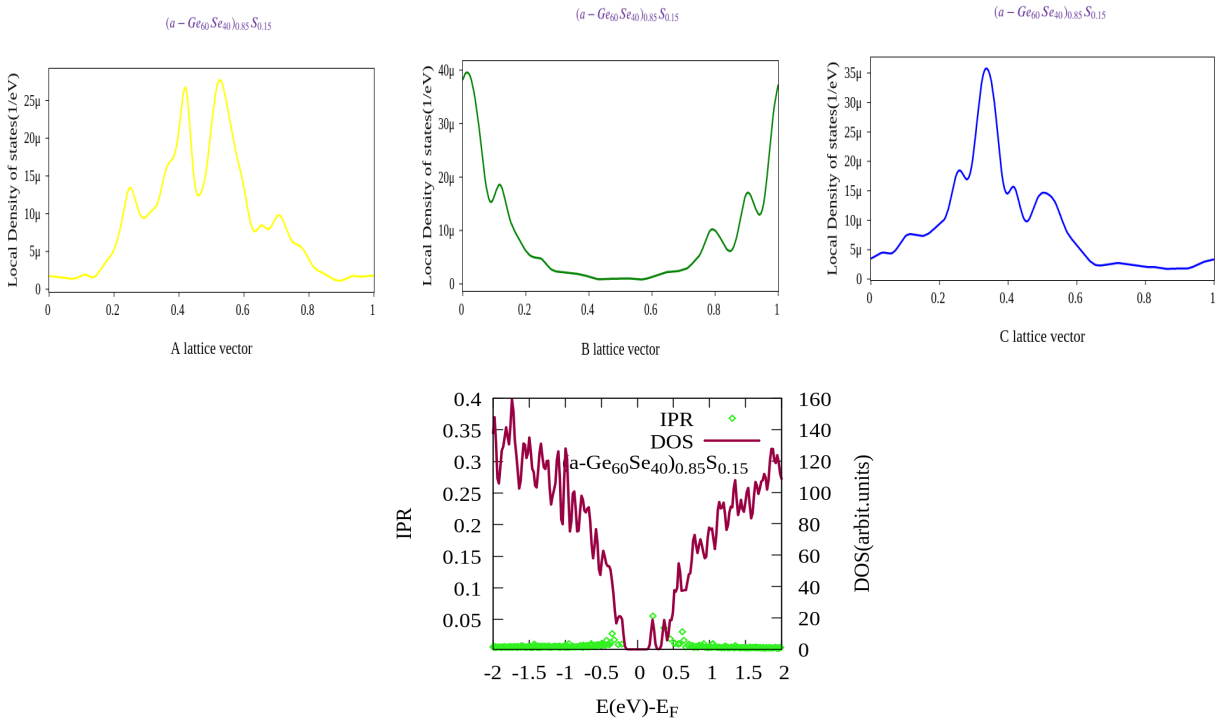

Figure 9. Top panel) The charge density of the in-gap state in a-$Ge_{60}Se_{40}S_{15}$ in the x,y,z direction, showing its spatial localization. Bottom panel) Total DOS and the Inverse Participation Ratio.

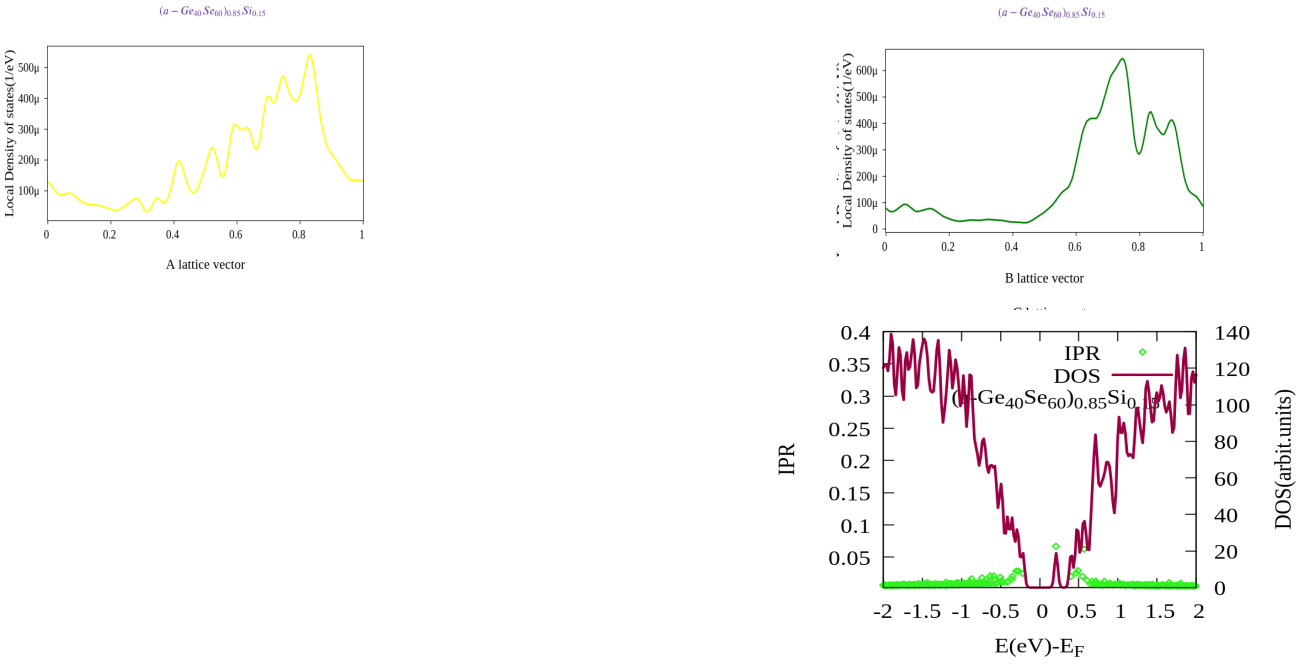

Figure 10. Top panel) The Local density of states of the localized in-gap state in a-$Ge_{40}Se_{60}S_{15}$ in the x,y,z direction. Bottom panel) Total DOS and the Inverse Participation Ratio.

3.2 Approach 2: Classical molecular dynamics + cell reduction

3.2.1 Structure generation

Step 1 - Classical MD simulation. The Ge_xSe_{1-x} systems have been simulated by using a classical molecular dynamics approach, along the lines introduced in D3.2 and reported in Ref. [6]. Three different stoichiometries have been simulated: $Ge_{0.4}Se_{0.6}$, $Ge_{0.5}Se_{0.5}$ and $Ge_{0.6}Se_{0.4}$. Each system contains 4480 atoms and the Force Field (FF) used is based on the well-established Vashishta potential employed for the description at the atomistic level of $GeSe_2$ or InP systems. The classical MD simulations have been carried out by using the LAMMPS package. Each model system has been melted for 10ns at 1500K and then slowly cooled down to 300K with a cooling rate of 5K/ps, which ensures a good balance between a low computational cost and a good description of the amorphous structure. Finally, a production run of 50ns at 300K has been carried out in a NVT ensemble where the temperature is controlled by the Nosé-Hoover thermostat with a coupling time of 1ofs and the timestep used is of 1fs.

The same simulation protocol of GeSe systems has been employed to produce the doped systems. In particular, for S, Si, and Te dopants, the force field employed is the Vashishta FF as for the GeSe systems where the new charges have been computed by the Rappe and Goddard's QEq scheme using the GULP package, ensuring the charge neutrality of the system. In the case of P Vashishta FF potential seems to be not accurate enough to account for the amphoteric character of the Ge-P and Se-P bonds. Thus, we generated a potential for P species to be used in the classical MD simulations. In order to test this new potential, we performed a set of ab initio DFT simulations on small systems, with 50 atoms/cell. The results have been used to fit the force field potential. The P dopant has thus been considered as a negative ion to reproduce the correct RDF of ab initio simulations and then the same procedure employed for S, Si, and Te is applied.

For the analysis of the structural properties, we developed a multi-technique numerical approach to study the order/disorder of amorphous materials on both the short- and the medium-range scale. We combine the analysis of the disorder level based on chemical and physical features (radial and angular distribution function, bond local order, XRD analysis), with their geometrical and topological properties (Voronoi tessellation and homology analysis), defining a previously unexplored interplay between the different techniques and the different order scales. The main features of this approach, summarized in Figure 11, have been reported in a paper to be published in ACS Omega (in press) [7].

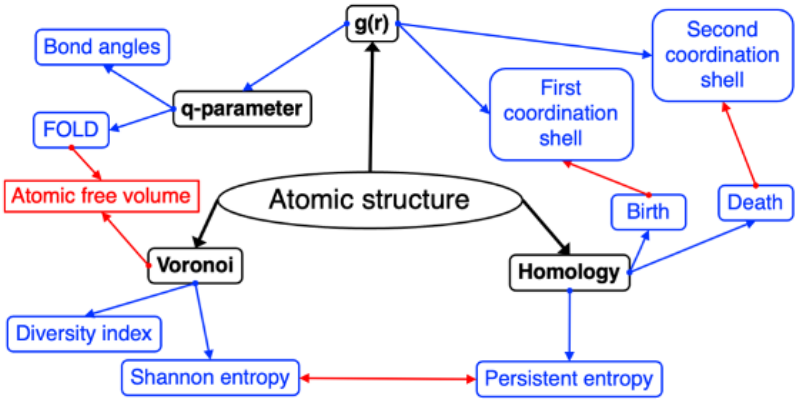

Figure 11. Sketch of the integrated multi-technique approach. The employed techniques are marked in bold, their output in blue, and the connections between them in red. Arrows identify the mutual dependencies. Picture from Ref. [7]

The development of this approach also required the implementation of an original code (named BELLO) for the evaluation of the q-parameter and the FOLD-ordered structures. The code is publicly available (https://github.com/behnood-dianat/BELLO) and its main features are described in a paper recently published in Comput. Mater. Sci [8] in collaboration with the AMAT team. This structural analysis tool is a byproduct of the INTERSECT project and has been considered as a key-exploitable product in the innovation management strategy discussed in Deliverables 4.7[4] and 4.8[5].

Step 2. System Reduction and DFT simulations.

Since simulation cells used in classical MD are too large for DFT calculations, we optimized a protocol to extract smaller, but structurally-reliable systems, affordable with DFT approaches (Figure 12).

[4] https://intersect-project.eu/wp-content/uploads/2022/04/D4.7.pdf
[5] https://intersect-project.eu/wp-content/uploads/2022/04/D4.8.pdf

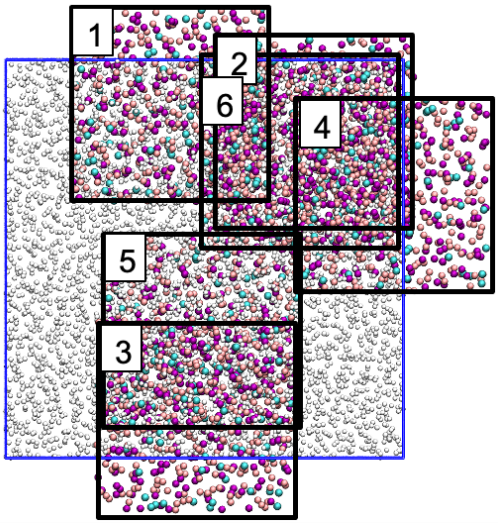

Figure 12. DFT small cell extraction from large MD systems.

For each system we extracted from the original MD trajectory 6 small cubic boxes of 500 atoms per cell with the same stoichiometry and the same density of the parent system. These smaller cells have been relaxed using MD at a constant temperature of 300K for 10ns in order to allow the broken bonds at the border to rearrange and match the new periodic boundary conditions. Each system has been further optimized at the DFT level, by using the Quantum ESPRESSO code. We further checked that the structural properties still reproduced the original ones. Finally, we used a DFT+U (see D3.2) approach to correct the well-known bandgap underestimation of standard DFT approaches.

3.2.2. Results

Undoped-GeSe. By using this MD+cell reduction approach, we performed a set of calculations to generate model structures for the three different stoichiometries corresponding to the experimental samples (D20, D21, and D22) fabricated by IMEC and discussed in D3.2, i.e., $Ge_{60}Se_{40}$, $Ge_{50}Se_{50}$, and $Ge_{60}Se_{40}$. The preliminary results on the structural properties of the undoped systems, as resulting from the MD simulations, have been already reported in D3.2 and in Refs. [6,7].

Figure 13 shows the radial distribution functions resulting from all the methods we applied to characterize these amorphous structures: the MD simulation on large cell (MD), DFT simulation on large cell (big cell), DFT results from quench-and-melt approach (q&m), and DFT from cell reduction (cut). A direct comparison clearly indicates that the final configurations resulting from the two approaches resemble the original one from classical MD, in particular the radial distribution functions are identical to the original results (*big cell*).

This confirms that we generated atomically different but statistically equivalent systems, whose structural characteristics are independent from the procedure and the numerical details used to realize the model. This is a very important result and the prerequisite to study electronic properties.

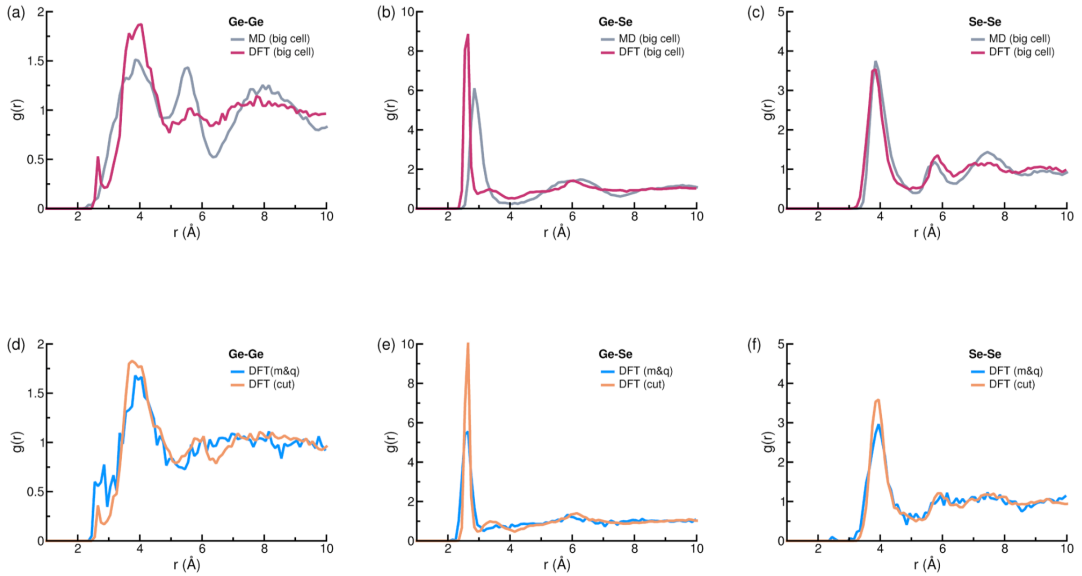

Figure 13. Radial distribution functions g(r) for (a,d) Ge-Ge, (b,e) Ge-Se, (c,f) Se-Se pair distances of $Ge_{50}Se_{50}$, simulated through different techniques.

For all GeSe compositions, twelve atomic structures have been generated to have a statistical meaningful insight of the amorphous characteristics. The DFT electronic structures of the single configurations are very similar for each stoichiometry. Figure 14 shows the DOS plot for one representative structure of $Ge_{50}Se_{50}$ and $Ge_{60}Se_{40}$, respectively, as resulting from this approach. The results well match those obtained with the alternative approach described in the previous Section.

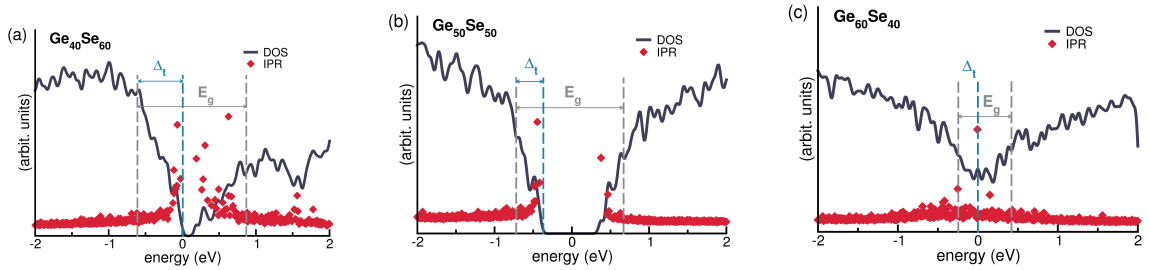

Figure 14. Density of States (DOS) plot for amorphous GeSe compounds at different stoichiometries. Red diamonds indicate the Inversion Participation Ratio (IPR) of single particle states. Vertical gray (cyan) dashed lines mark the mobility gap E_g (trap band Δ_t) of the system. The zero-energy reference is set to the Fermi level of each system.

Doped-GeSe. By using MD approach, we simulated a series of doped a-$(Ge_xSe_{1-x})_{1-y}D_y$ systems, by varying both the stoichiometry (x=0.4, 0.5, 0.6), the dopants (D=Si, S, Te), and their concentrations (y= 1%, 3%, 5%,7%, 10%, 15%) on large cell with 4480 atoms per cell. Simulations for P-doped aGeSe are still in progress. The main structural properties for Si and S dopants are summarized in Figure 15.

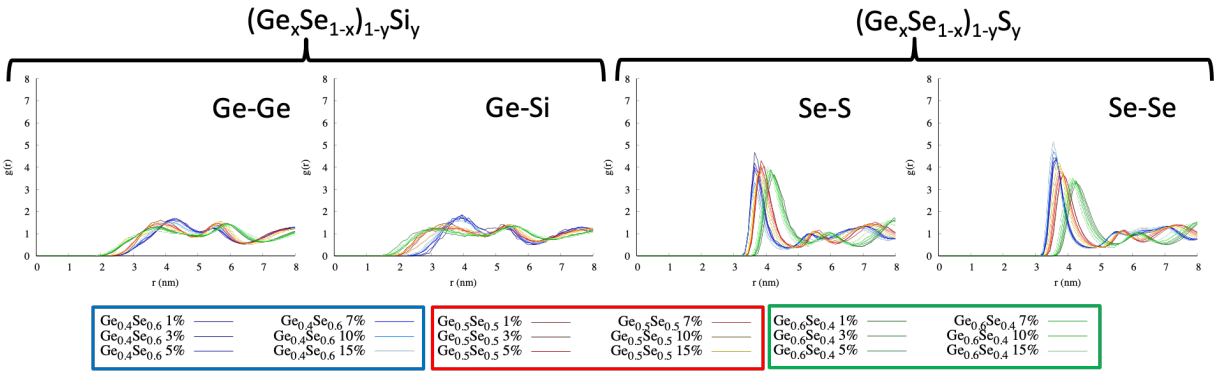

Figure 15. Radial distribution function for $(Ge_xSe_{1-x})_{1-y}Si_y$ and $(Ge_xSe_{1-x})_{1-y}Si_y$ at different dopant concentrations, as resulting from classical MD simulation on large cells.

Apart from the specific details of each system, we obtain that RDF (or g(r)) of Ge-Te and Ge-S are similar to Ge-Se, while g(r) of Ge-Si is similar to Ge-Ge, which means Te and S are similar to Se, while Si is similar to Ge. Indeed, the former are all chalcogenides, the latter are Group IV elements. We can conclude that the short-range order is dominated by heteropolar bonds. These results are in very good agreement with the ones obtained in the previous section.

We use the Voronoi tessellation and the homology analysis to investigate the medium range order. Figure 16 shows the results for the case $(Ge_{0.5}Se_{0.5})_{0.85}Te_{0.15}$ that indicate a dependence of the structural order on the dopant type, dopant concentration, GeSe stoichiometry. In general, Se-rich are less ordered than Ge-rich systems, and Si-doped are less ordered than S/Te-doped systems, respectively. We assumed these structural parameters as the reference to check the "quality" of the model used for DFT simulations performed both with SIESTA (see above) and QE.

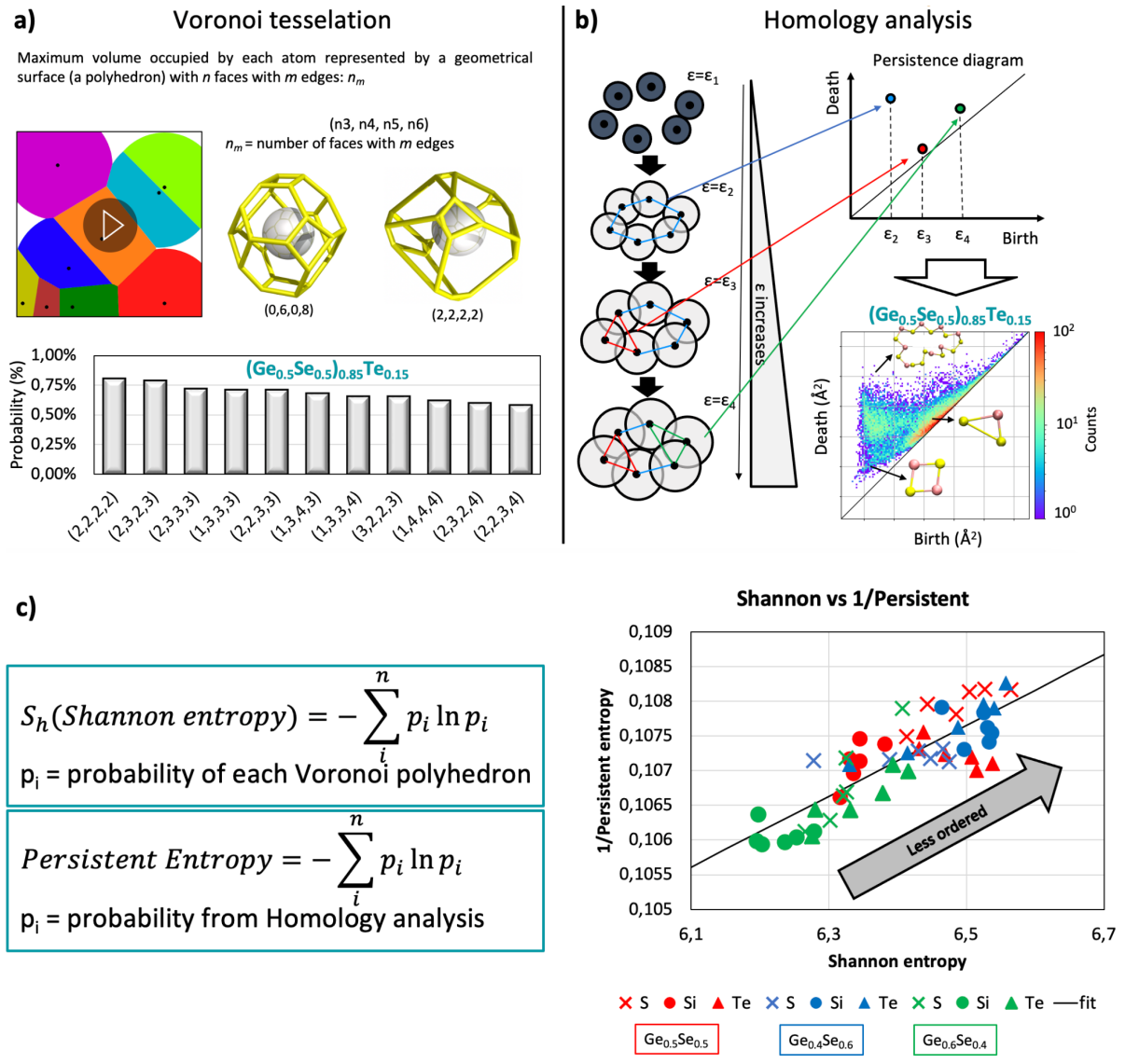

Figure 16. Medium-range structural characterization of amorphous structures from MD simulations, based on Voronoi tessellation and Homology analysis.

After applying the "cut" protocol discussed above to reduce the size of the simulation cell, we calculated the electronic properties of doped a-$(Ge_xSe_{1-x})_{1-y}D_y$ compounds (six configurations per system). The average mobility bandgaps for selected systems are reported in Table II. Bandgaps are among the materials parameters used as input for the device simulations (see next Section).

Table II. Bandgap of selected a-$(Ge_xSe_{1-x})_{1-y}D_y$ systems.

System	Dopant	Concentration	Bandgap (eV)
Ge40Se60	undoped	0%	1,338
Ge50Se50	undoped	0%	1,373
Ge60Se40	undoped	0%	0,760
Si-Ge50Se50 (1-pc)	Si	1%	0,978
Si-Ge50Se50 (5-pc)	Si	5%	0,948
Si-Ge50Se50 (10-pc)	Si	10%	0,768
Si-Ge60Se40 (1-pc)	Si	1%	0,612
Si-Ge60Se40 (5-pc)	Si	5%	0,592
Si-Ge60Se40 (10-pc)	Si	10%	0,632
S-Ge50Se50 (5-pc)	S	5%	1,187
S-Ge60Se40 (5-pc)	S	5%	0,774
Te-Ge50-Se50 (5-pc)	Te	5%	0,993
Te-Ge60-Se40 (5-pc)	Te	5%	0,750

In view of the multiple degrees of freedom, in Figure 17 we present a few comparative analyses of the electronic structure of selected systems, in order to investigate the role of the concentration at fixed stoichiometry (top panel), the effect of stoichiometry at fixed dopant concentration (central panel), and the effect of the dopant choice at fixed concentrations (bottom panel). This comparison indicates that: (i) in view of the similar behavior of Si and Ge, increasing the Si concentration provides electronic structures similar to a−$Ge_{0.6}Se_{0.4;}$ (ii) in

$Ge_{0.4}Se_{0.6}$ the localized states are closer to conduction band, while in $Ge_{0.6}Se_{0.4}$ Si reduces the mobility gap; (iii) $(Ge_{0.5}Se_{0.5})_{0.95}Te_{0.05}$ is similar to $(Ge_{0.4}Se_{0.6})_{0.95}Si_{0.05}$. (iv) the number and the energy position of localized states (traps) varies mostly with the Ge/Se stoichiometry of the system. $Ge_{0.5}Se_{0.5}$ compounds have open bandgap with a few trap states close to band edges, while Ge-rich systems have several localized states that occupy the entire band gap region.

The comparison between the results obtained with SIESTA and QE indicate that even though the specific choice of the numerical details (e.g., exchange-correlation functional) may affect the quantitative value of parameters such as the bandgap, both DFT approaches give the same qualitative results. This assures that the trap states analysis is robust and independent from the specific choice of the used DFT code. A joint paper with the results of the doped systems is in preparation.

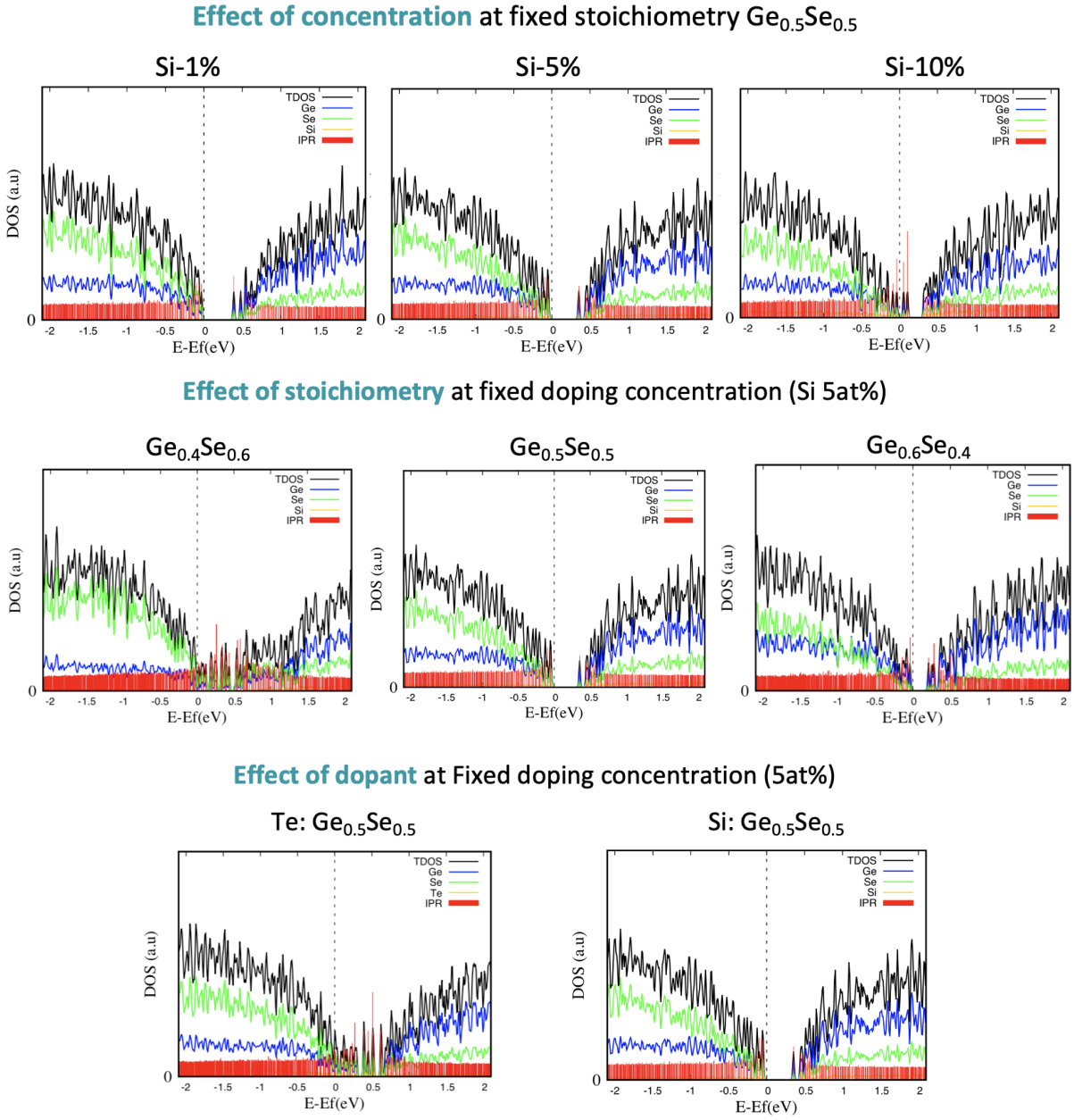

Figure 17. Comparative analysis of the electronic structure of doped a-$(Ge_xSe_{1-x})_{1-y}D_y$ systems as a function of the concentration (top panel), stoichiometry (central panel), and dopant species (bottom panel). Black line is the total DOS; blue, green, and orange lines are the projected DOS on Ge, Se, and dopant, respectively. Red lines mark the IPR for each system. Vertical dotted lines identify the Fermi level of the system.

3.3 TiN/amorphous interfaces

One relevant parameter that enters as input in the simulation of the selector device (see next Section) is the work-function (WF) of the TiN electrodes, upon the formation of the interface with the amorphous layer. The experimental results presented in D3.2 showed that the thickness of the GeSe layer plays a role in the electrical characteristics of the selectors, as well as they pointed out that the inclusion of a-Carbon (a-C) layer between the TiN and the a-GeSe layer may turn the electrical character of the interface from Schottky to Ohmic. We previously investigated the modifications of the TiN work-function as a function of the exposed surface, of the thickness and of possible N-vacancies (see D2.3 [6]and Ref. [9]).

Here, we present the results about the TIN WF changes due to the contact formation with a-GeSe and a-C. This work has been done in collaboration with the IMEC group. Figure 18 summarizes the interface structures considered in this study, namely TiN(111)/a-GeSe, TiN(100)/a-GeSe, and TiN(111)/a-C with different thickness for a-GeSe layers.

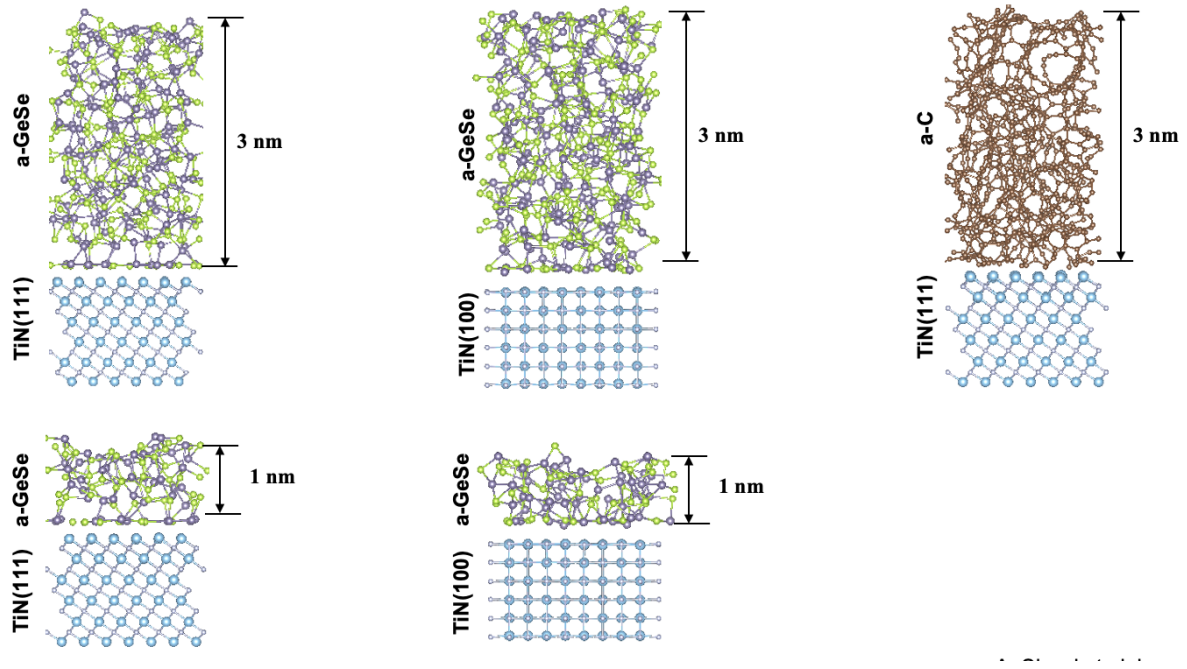

Figure 18. Interfaces of TiN with a-GeSe and a-C layers.

[6] https://intersect-project.eu/wp-content/uploads/2022/04/D2.3.pdf

The band alignment of the isolated sub-systems (Figure 19, left) indicates that the work-function of TiN(100) is too low to be a good contact for GeSe. On the contrary, the work-function of TiN(111) lies in the energy gap of both a-GeSe and a-C systems. The formation of the interface pins the Fermi Level of the systems (i.e., the effective WF of the metal in the device configuration) in the middle of the a-GeSe bandgap (right panel). This is a fingerprint of the formation of a Schottky barrier at the interface. Different is the case of TiN/a-C where the resulting Fermi level is degenerate to the edge of the carbon conduction band, which is typical of a Ohmic-like contact, in agreement with the experimental evidence. The analysis of the electronic structure indicates that the different electric behaviour between the two systems is related to the formation of a "wetting layer" that in the case of a-GeSe reduces the bond formation at the interface. At odd, the bond-saturation is more effective in the case of a-C and the formation of mixed TiN/C states at the interface pins the Fermi level on the bottom of the conduction band.

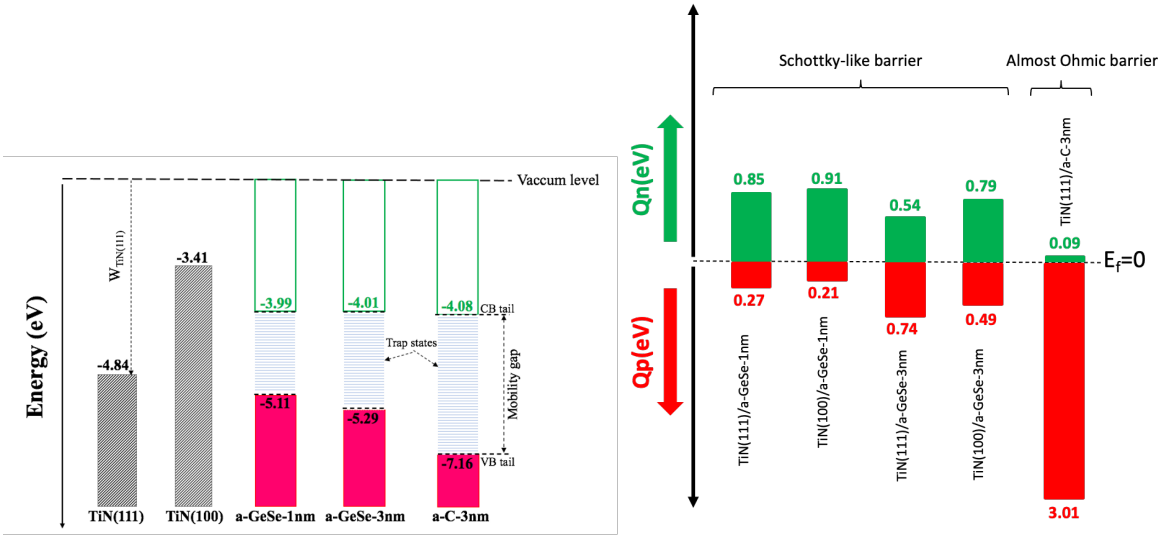

Figure 19. (left) Band-alignment diagram, (right) barrier formation aa the interface.

The main structural and electronic properties of the TiN/amorphous interfaces are summarized in Table III, where d is bonding distance, E_b is the binding energy, Φ_n and Φ_p are the Schottky barriers for electrons and holes, respectively. These results have been collected and a manuscript is in preparation.

Table III. Selected structural and electronic properties of the TiN/amorphous interfaces.

Interface	d (Å)	E_b (meV/A^2)	Φ_n (eV)	Φ_p (eV)
TiN(111)/GeSe-1nm	2.13	-264.54	0.85	0.27
TiN(111)/GeSe-3nm	2.08	-297.65	0.54	0.74
TiN(100)/GeSe-1nm	2.16	-83.39	0.91	0.21
TiN(100)/GeSe-3nm	2.58	-96.22	0.79	0.49
TiN(111)/Carbon-3nm	1.31	-364.47	0.09	3.01

The main materials properties of doped a-GeSe and the electrical parameters of the contacts (e.g., WF, and Φ_p) are shared with the AMAT team for the simulation of the OTS devices.

4. DFT-based OTS Device Simulations

4.1 Ginestra® OTS Model

The Ovonic Threshold Switching (OTS) is a peculiar feature exhibited by amorphous chalcogenides that reversibly switch from a low-conductance to a high-conductance state triggered by the electric field. The unique and distinctive OTS model implemented in Ginestra® extends the description of the trap assisted charge transport through the material with the hydrodynamic approach of [10], by coupling the charge continuity equation

$$f_i \sum_{j \neq i} (1 - f_j) R_{ij} = (1 - f_j) \sum_{j \neq i} f_j R_{ji} \quad (1)$$

with the energy-continuity equation

$$(1-f_i)\sum_{j\neq i} f_j R_{ji}\left(e_j - e_i - q\Delta V_{ij}\right) - f_i e_i \sum_{j\neq i}\left(1-f_j\right)R_{ij} = f_i\frac{e_i - e_{i0}}{\tau} \quad (2)$$

where f_i and R_{ji} indicate the occupation of *i*-th defect and the transition rate from the *i*-th to *j*-th trap, respectively. The energy flux balance in (2) involves the energy gain due to the local electric field and the losses associated with phonon interaction where e_i denotes the carrier energy at the *i*-th trap site with ground energy e_{i0}. τ is the energy relaxation-time constant that defines the time required to relax the carriers' excess energy (e_i - e_{i0}) to the lattice. If τ = 0, any excess energy is immediately relaxed (e_i = e_{i0}), and the defect behaves as a standard defect, preventing the onset of OTS. On the contrary, the larger τ the higher the energy gained, and the lesser the electric field required to trigger the transition to the high-conductance state.

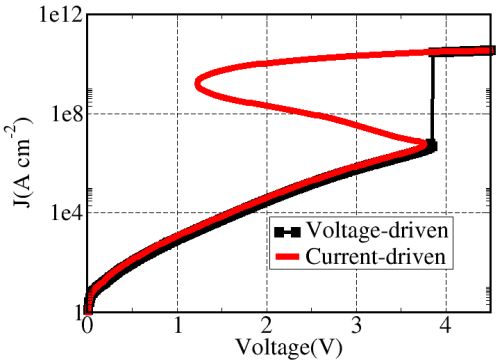

Figure 20. Current-Voltage characteristic simulated using th for the (black line) voltage-driven and (red line) current-driven mode.

Figure 20 shows an example of current-voltage characteristics simulated under voltage- and current-driven operations using the described OTS model. In the voltage-driven response (black line), two different conductive regions (i.e., ON and OFF) are separated by an abrupt increase in current caused by a large drop of resistivity. In the current-driven response (red line in Figure 20), we can identify three different conductive regions: the OFF state at low fields, a switching regime characterized by a voltage-snapback with a negative differential resistance, and a high current ON state. These three regimes are obtained through the

coupled solution of Eq. (1)-(2) and can be interpreted in relation to the trap-assisted conduction and the excess carriers' energy diagrams reported in Figure 21.

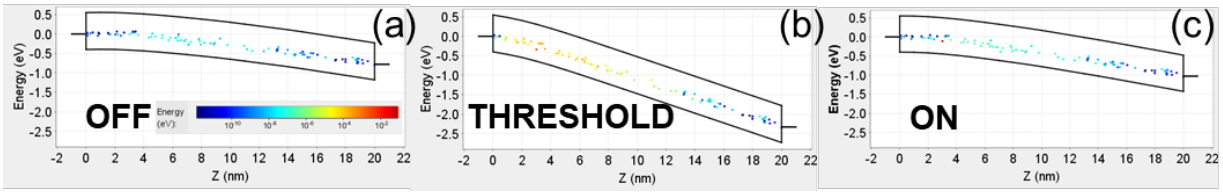

Figure 21. Band diagram with defect excess energy evaluated for the OFF state (a), threshold (b) and ON state (c).

In the OFF state, Figure 21a, the current is due to multi-phonon trap-assisted transport (TAT) with no carrier heating. The accurate modeling of this trap-assisted conduction demands for an accurate description of OTS defects (in terms of atomic structure and properties to be used in device simulations), a need that can be satisfied by both the device-to-material (see D3.2) and the material-to-device (see below) cycles of the IM2D simulation box. For increasing voltages, Figure 21b, the carriers progressively fail to entirely relax their excess energy (calculated through the coupled solution of charge-continuity and energy-continuity equations) to the lattice and become hot. This electric-field induced carrier heating triggers a temporary and progressive transformation from localized to delocalized states, creating highly conductive pathways immersed in a low-conductive matrix. In this regime, carriers can sustain higher currents with lower fields, thus resulting in a current increase for decreasing voltages. In the ON state, Figure 21c, the structural reorder of bonds is assumed to yield highly conductive defect-states featuring an excess energy significantly higher than those of the other defects. This results in a typical filamentary conduction mechanism, in agreement with the theoretical expectations. When the bias voltage (or current) is reduced, the excess energy is again effectively released to the lattice, the delocalized states switch back into localized defects, and the system recovers the original OFF state.

4.2 OTS Simulations: Calibration on undoped GeSe films

We first used the Ginestra® OTS model to reproduce voltage-driven OTS switching characteristics measured on metal/insulator/metal (MIM) capacitors with undoped GeSe films with different stoichiometries. Material and trap parameters used in simulations are the ones derived by applying the Ginestra® DDT tool as described in D3.2.

Figure 22 shows the results of the simulations and their comparison with the measured electrical OTS switching data. As it can be seen, our numerical outputs agree very well with

measurements both in the OFF and ON states. Moreover, they provide an accurate estimate of the switching voltage that is found to vary with composition.

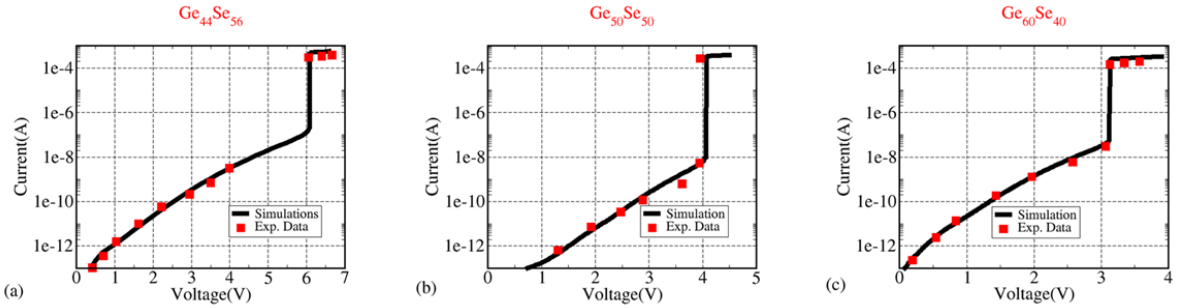

Figure 22. Voltage-driven experimental (red squares) and simulated (black lines) I(V) curves for different composition stoichiometries of GeSe; namely (a) $Ge_{44}Se_{56}$, (b) $Ge_{50}Se_{50}$, and (c) $Ge_{60}Se_{40}$.

These initial simulations allowed us to calibrate and validate the OTS model, which is an important step for having reliable and predictive simulations based on DFT calculation as the ones presented in the next Section.

4.3 OTS Simulations: OTS switching in Si-doped GeSe films

The OTS model described in Section 4.1 has been used to evaluate the impact of material and trap parameters on device electrical characteristics. As a case study, we considered here the results obtained for a 20nm-thick TiN/$Ge_{50}Se_{50}$/TiN OTS stack with different Si doping concentrations of 1%, 5% and 10%.

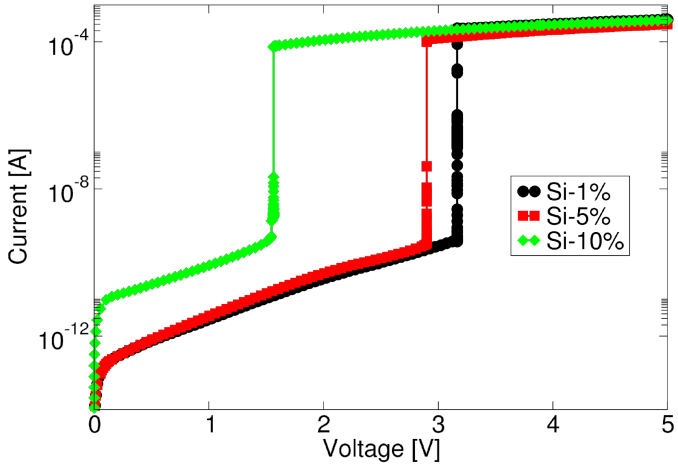

Figure 23. Voltage-driven OTS switching characteristics simulated for $Ge_{50}Se_{50}$ samples with Si doping concentration of (black circles) 1%, (red squares) 5%, and (green diamonds) 10%.

The material bandgap (decreasing from ~0.98eV to ~0.77eV for Si-doping concentration increasing from 1% to 10%, Table II), and the defect properties (slightly affected by the doping concentration), and the TiN effective WF calculated in Section 3 through DFT methods are taken as inputs to the device simulations.

Figure 23 shows the simulated voltage-driven switching characteristics for the considered Si doping concentrations. DFT-based device simulation results highlight three main aspects:

- the leakage current strongly increases with increasing doping concentration,
- the switching voltage (that is, the voltage at which the OFF to ON transition is observed) strongly reduces with increasing Si doping concentration,
- the ON state current is not affected by Si doping.

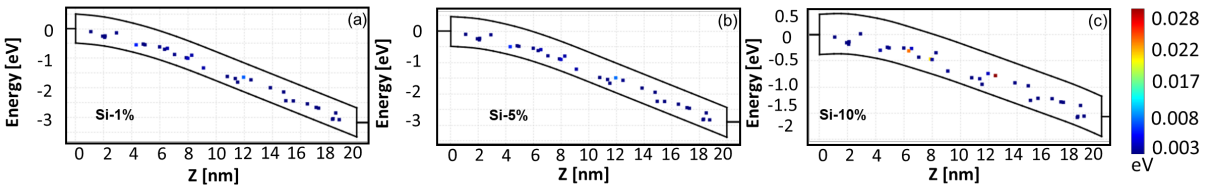

Figure 24. Band diagram of the simulated OTS devices showing carriers' excess energy at trap sites, evaluated at the switching threshold voltage for Si doping concentrations of (a) 1%, (b) 5%, and (c) 10%.

Simulation results can be easily understood by looking at the carriers' energy and current distribution at threshold and ON state, respectively. Figure 24 shows the devices band diagrams with the carriers' excess energy at trap sites, as determined by the simulations at the switching threshold voltage. The average carriers' energy is higher in the devices with a

higher Si doping concentration, which results in the observed reduction of the switching voltage. This behaviour is determined by the reduction of the GeSe bandgap that, together with the very similar properties of the GeSe traps calculated for the different Si doping levels (that is, they remain close to the midgap region and aligned with the TiN metal work-function), determines a reduction of the height of the energy barrier that carriers encounter during their trap-assisted conduction through the film. Therefore, the tunneling process becomes more favorable and faster than the time required to relax the carriers' excess energy to the trap sites [determined by the relaxation time constant in Eq. (2)], making carriers become more energetic (*hot*). Note that the bandgap reduction is also responsible for the observed increase of the OFF current.

Finally, simulation results also show that the ON state current is not affected significantly by the Si doping concentration. Figure 25 shows a 3D view of the simulated OTS devices in the ON state, highlighting the current driven by the defects. For higher dopant concentrations, fewer traps are found to contribute to the filamentary conduction mechanisms.

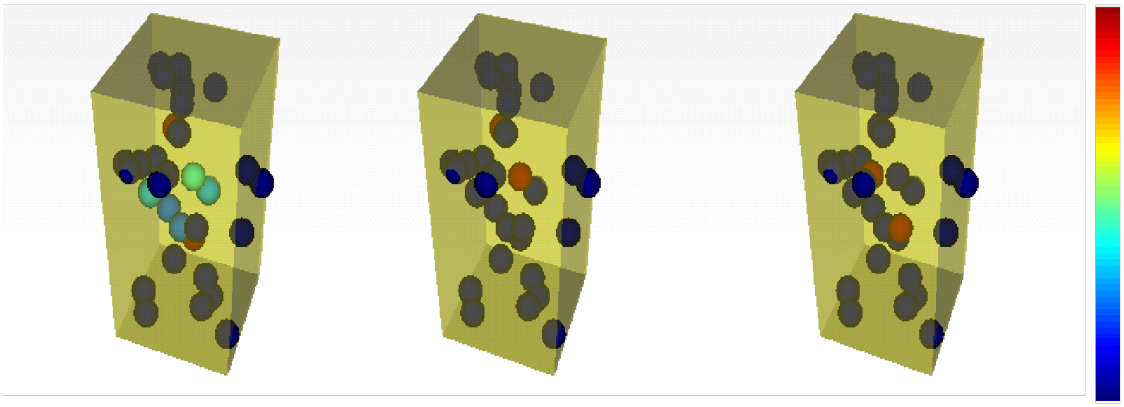

Figure 25. 3D view of the simulated OTS devices in the ON state, highlighting the current filament formed by the most conductive defects. A reduction of the number of traps forming the filament is observed at higher Si doping concentration.

Overall, the DFT-based OTS device simulations discussed here, and performed within the framework of the M2D workflow of the IM2D simulation box, highlight some important aspects related to GeSe doping (with Si):

- higher doping concentration is desirable to reduce the switching voltage (thus enabling low-power operations), but at the same time leads to an increase of the OFF-state current, which is not desirable as it increases the device/array power

dissipation. This important trade-off has to be taken into account when designing the device and the memory array,

- the reduction of the GeSe traps responsible for the ON-state conduction is expected to affect (increase) device-to-device variability, which is critical for device scaling and integration into ultra-dense non-volatile memory arrays.

Conclusions

This deliverable summarized the activity of Task 3.4 about the M2D workflows for the optimization of selector device performances, through the materials workspace exploration based on quantum mechanical simulations by DFT. Huge efforts have been dedicated to the definition of numerical protocols for the generation of atomistic models that can represent the amorphous materials with sufficient fidelity. This allowed us to unravel the interplay between local-order structures, trap states, and the resulting electrical response for a-GeSe systems, by spanning different stoichiometries, dopant species, and dopant concentrations.

The results we presented demonstrate that the IM2D provides a very useful and effective way to assess and predict the impact of material and trap properties variations on the device electrical behavior. This can be used for an effective pre-screening of potential process/technology solutions and for the virtualization of the fabrication process eventually resulting in a huge reduction of fabrication costs and time-to-market reduction.

References

[1] Burr et al., J. Vac. Sci. Technol. B **28,** 223 (2010).
[2] Wang et al., Review@RRL **13**, 1900073 (2019).
[3] Aluguri et al., IEEE J. Electron Devices Soc. 4, 294 (2016).
[4] Chen, 2013 13th Non-Volatile Memory Technology Symposium (NVMTS).
[5] Liu et al., ACS Appl. Nano Mater. **2**, 5373 (2019).
[6] F. Tavanti et al., ACS Appl. Elec. Mater. **2**, 2961 (2020).
[7] F. Tavanti and A. Calzolari, ACS Omega (2022), in press.
[8] B. Dianat et al., Compt. Mater. Sci. **209**, 111381 (2022).
[9] A. Calzolari et al., IEEE Access **8**, 156308 (2020).
[10] A. Cappelli et al., Appl. Phys. Lett. **103**, 083503 (2003).

Acronyms

ADF - Angle Distribution Function
COHP - Crystal Orbital Hamilton Populations
DFT - Density Functional Theory
DOS - Density of States
D2M- Device-To-Material
FF - Force Field
IM2D - Interoperable Materials to Device
IPR - Inverse Partition Ratio
MCMC - Metropolis Markov Chain Monte Carlo
MD - Molecular Dynamics
MIM - Metal-Insulator-Metal
M2D - Material-To-Device
OTS - Ovonic Threshold Switching
QE - Quantum Espresso
RDF - Radial Distribution Function
TAT - Trap Assisted Transport
WF - Work-function